Supporting Information

Pollen Typhae-Based Magnetic-Powered Microrobots toward Acute Gastric Bleeding Treatment

Qingxin Yang,[†] *Songsong Tang,*[*,†] *Dongdong Lu,*[†] *Yangyang Li,*[†] *Fangchen Wan,*[†] *Jiahong Li,*[‡] *Qiwei Chen,*[†] *Zhaoqing Cong,*[†] *Xueji Zhang,*[§] *Song Wu*[*,†,¶]

[†]Institute of Urology, The Third Affiliated Hospital of Shenzhen University, Luohu Hospital Group, Shenzhen 518000, P. R. China

[‡]Andrew and Peggy Cherng Department of Medical Engineering, California Institute of Technology, Pasadena, California 91125, United States

[§]School of Biomedical Engineering, Health Science Center, Shenzhen University, Shenzhen 518060, P. R. China

[¶]South China Hospital, Shenzhen University, Shenzhen 518116, P. R. China

Corresponding Authors

*Email: songsong.tang@hotmail.com (S.T.)

*Email: wusong@szu.edu.cn (S.W.)

Supporting videos:

Movie S1: Propulsion performance of PT robots upon RMF control with different intensities

Movie S2: Propulsion performance of PT robots upon RMF control with different frequencies

Movie S3: Propulsion performance of PT robots in various biological media upon RMF control

Movie S4: Motion trajectory of the PT robot upon a predefined recantgle-like path

Supporting Figures:

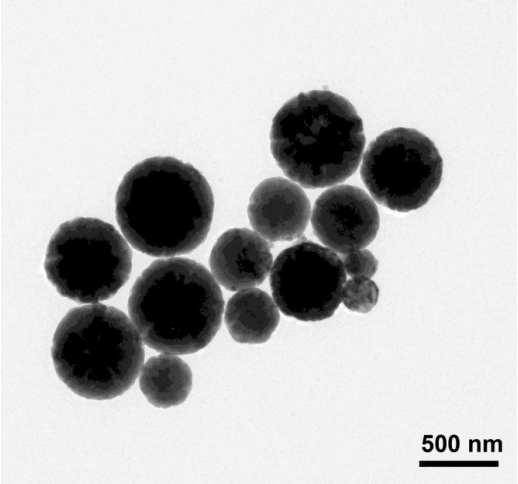

Figure S1. TEM images of fabricated Fe_3O_4 NPs.

Figure S2. Images of PT solutions before (left, yellow) and after (right, black) dip-coating process with Fe_3O_4 NPs.

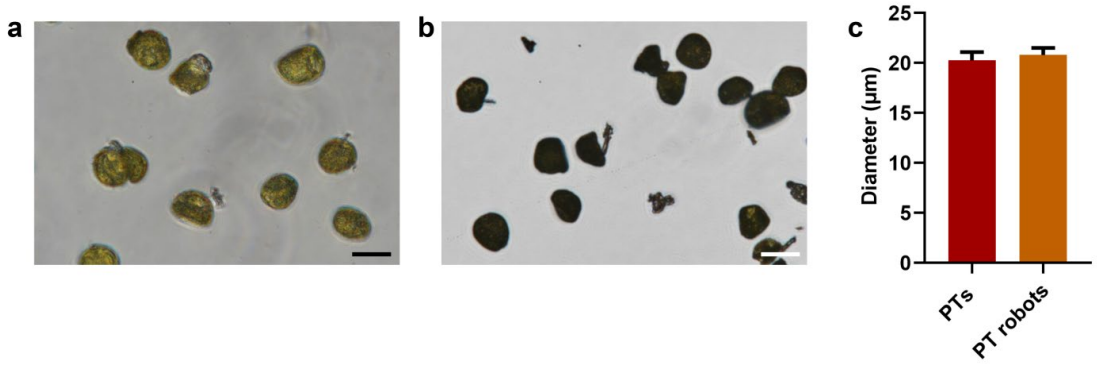

Figure S3. Optical images of PT microparticles (a) before and (b) after coating Fe_3O_4 NPs; and (c) their size changes. Scale bar: 20 μm.

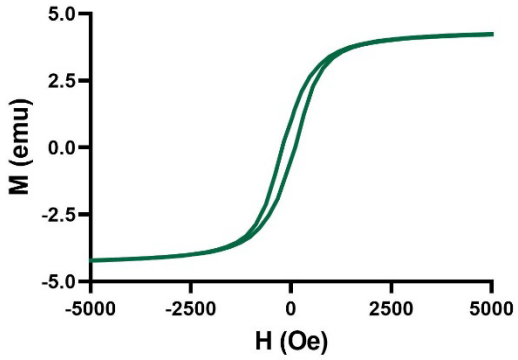

Figure S4. Magnetic hysteresis loop of PT robots.

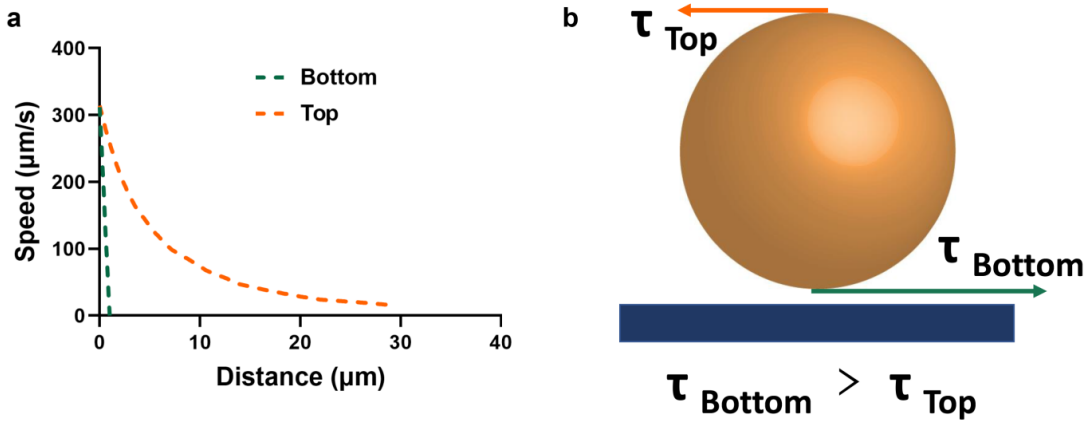

Figure S5. (a) Fluid flow velocity at various distance to the top and bottom of PT robot and (b) corresponding mismatched hydrodynamic shear force on two side, where $\tau_{bottom} > \tau_{top}$.

The fluid flow on the bottom of PT robot was hampered because of the no-slip condition. Figure S4a displays the relationship between the fluid flow speed and distance to the top or bottom surface of PT robot, revealing that the velocity gradient below the PT robot was much higher than the top part. It means:

$$\left|\frac{\partial U_{bottom}}{\partial d}\right| > \left|\frac{\partial top}{\partial d}\right| \quad (1)$$

Where U_{top}, U_{bottom} and d represent fluid velocity above the PT robot, fluid velocity below the PT robot, and distance to the surface, respectively.

The shear force acting on the top (τ_{top})and bottom (τ_{bottom}) of PT robot can be defined as:

$$\tau_{top} = -\mu \frac{\partial U_{top}}{\partial d} \quad (2)$$

$$\tau_{bottom} = -\mu \frac{\partial U_{bottom}}{\partial d} \quad (3)$$

Where μ denote the viscosity coefficient of fluid. Due to the result in equation (1), then:

$$|\tau_{bottom}| > |\tau_{top}| \quad (4)$$

Therefore, the counteraction of mismatched hydrodynamic shear force on two side of PT robot can generate a net propulsive force, turning the rotation to linear movement.

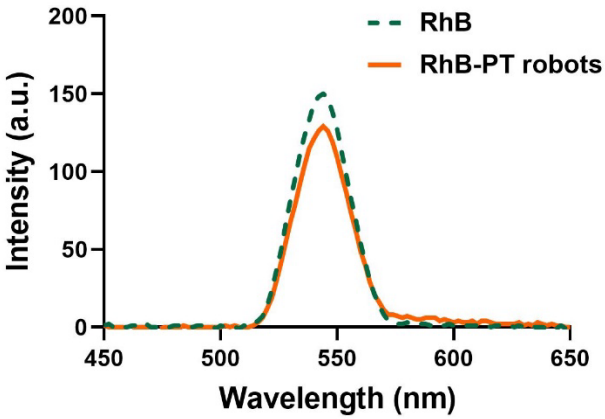

Figure S6. Fluorescent emission spectrum of RhB and RhB-labelled PT robots.

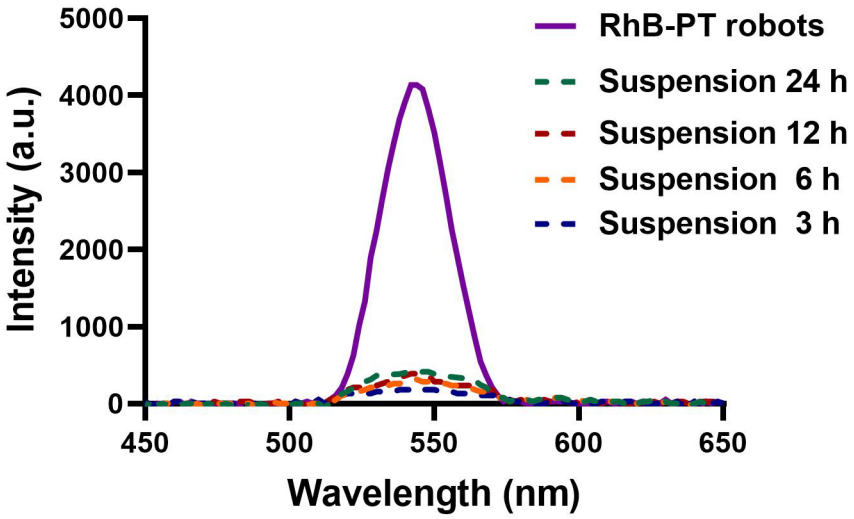

Figure S7. Fluorescent intensity of RhB-labelled PT robots and the suspension that incubated with RhB-labelled PT robots for 3, 6, 12 and 24 hours.

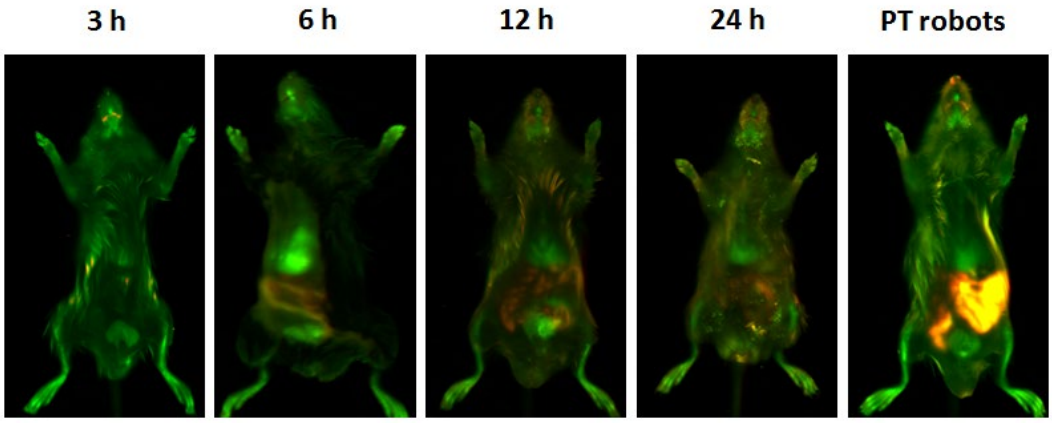

Figure S8. In vivo fluorescent imaging of mice that orally administrated with RhB-labelled PT robots and the suspension that incubated with RhB-labelled PT robots for 3, 6, 12 and 24 hours.

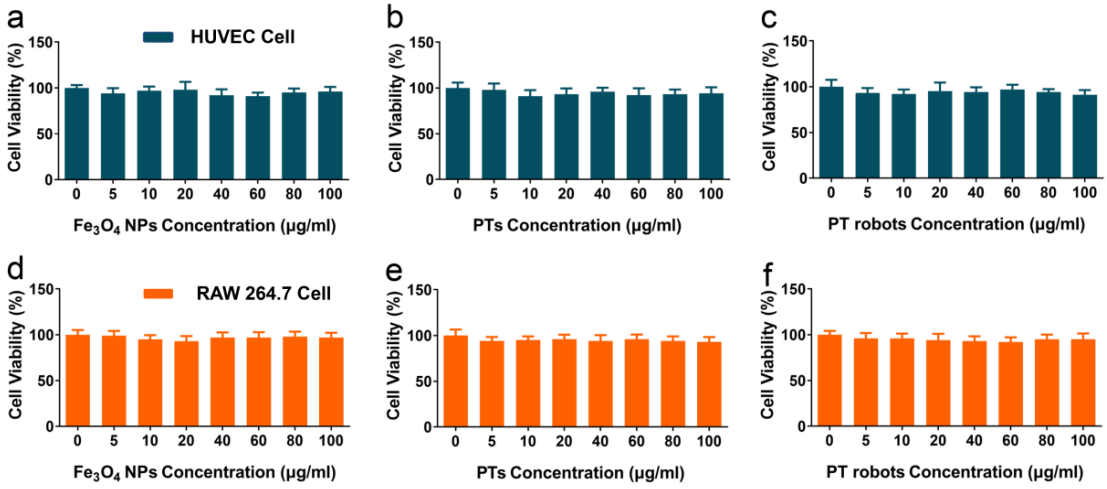

Figure S9. Cytotoxicity of Fe_3O_4 NPs, PTs and PT robots upon various concentrations toward (a-c) HUVEC and (d-f) RAW264.7 cell.

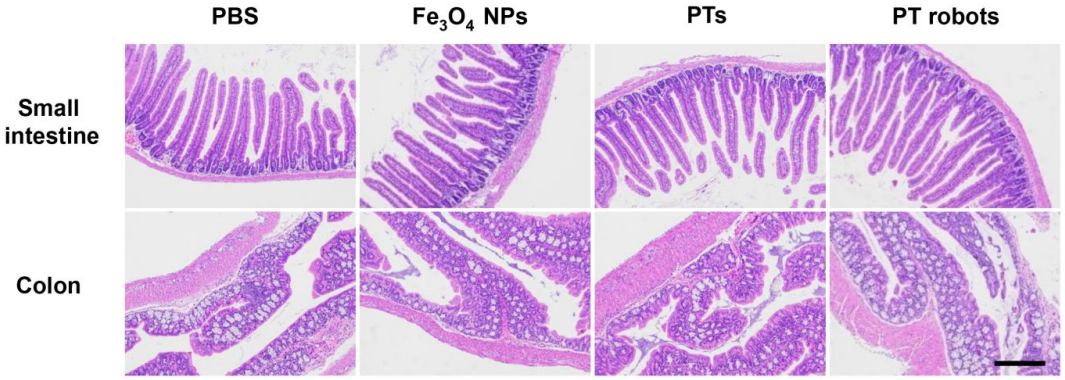

Figure S10. H&E staining of small intestine and colon sections dissected from healthy mice after various oral administrations for 5 consecutive days. Scale bar: 300 μm.